Aerospace Science and Technology 93 (2019) 105186

Contents lists available at ScienceDirect

Aerospace Science and Technology

www.elsevier.com/locate/aescte

Parametric design of non-axisymmetric separate-jet aero-engine exhaust systems

John J. Otter [a,*], Robert Christie [a], Ioannis Goulos [a], David G. MacManus [a], Nicholas Grech [b]

[a] Centre for Propulsion Engineering, School of Aerospace, Transport and Manufacturing, Cranfield University, Bedfordshire, MK43 0AL, UK
[b] Installation Aerodynamics, Rolls-Royce plc, Derby, UK

ARTICLE INFO

Article history:
Received 29 November 2018
Received in revised form 11 March 2019
Accepted 13 May 2019
Available online 16 July 2019

Keywords:
Exhaust nozzle
Class Shape Transformation
Non-axisymmetric
Aero-engine
Computational fluid dynamics
Propulsion integration

ABSTRACT

Future civil air vehicles are likely to feature propulsion systems which are more closely integrated with the airframe. For a podded underwing configuration, this close coupling is expected to require non-axisymmetric design capabilities for the aero-engine exhaust system. This work presents the development of a novel parametric representation of non-axisymmetric aero-engine exhaust system geometries based on Intuitive Class Shape Transformation (iCST) curves. An exhaust design method was established and aerodynamic analyses of a range of non-axisymmetric configurations was demonstrated. At typical flight conditions, the introduction of non-axisymmetric separate-jet nozzles was shown to increase the engine net propulsive force by 0.12% relative to an axisymmetric nozzle.

© 2019 Rolls-Royce plc. Published by Elsevier Masson SAS. This is an open access article under the CC BY license (http://creativecommons.org/licenses/by/4.0/).

1. Introduction

The reduction of engine specific fuel consumption (SFC) is a major focus in the design and development of aero-engines: the aerodynamic performance of the exhaust system is central to this aim. Future engines are expected to operate with low Fan Pressure Ratios [1], high bypass ratios (BPR) [2] and low specific thrust in order to increase propulsive efficiency and hence reduce specific fuel consumption (SFC) [3]. As a result of these changes in operating point, the overall engine efficiency for future engine configurations will become more dependent upon the aerodynamic performance of the exhaust system [4].

The primary aim of much of the previous research into single stream non-axisymmetric exhaust nozzles is on the enhancement of jet mixing [5–7] with multiple applications to military aircraft demonstrated [8–10]. For civil applications the focus of previous non-axisymmetric separate-jet nozzle studies has been on jet noise reduction: examples include chevron nozzles [11], elliptical core nozzles [12], elliptical bypass nozzles [13] and deflection of the bypass jet with nozzle guide vanes [14]. However, the impact of non-axisymmetric designs on the aerodynamic performance of a separate-jet exhaust nozzle has not yet been reported in the open literature.

In addition to noise reduction, non-axisymmetric nozzle designs for civil aircraft may be required to facilitate the integration of an engine onto an airframe. The installation of a conventional podded engine onto an aircraft is known to increase drag [15,16] and the aerodynamic design of the nacelle can reduce such interference [17,18]. Furthermore, as future aero-engines are expected to feature an increase in engine fan diameters, it is likely that future engine installation positions are to be closer to the wing. As a result, the trailing edge of the bypass nozzle may need to be non-circular to achieve a required local clearance between the engine and airframe. Moreover, non-axisymmetric nozzles provide a way to mitigate adverse three-dimensional flow features as well as accommodating close coupled integration between the engine and the aircraft wing.

The ability to perform effective aerodynamic shape optimisation is heavily dependent upon the method which is used to control the geometry [19]. One increasingly flexible method for the parameterisation of aerofoils is the Class Shape Transformation (CST) approach proposed by Kulfan [20,21]. Moreover, multiple studies have been conducted which perform aerodynamic shape optimisation with a CST based parameterisation approach [22–24]. The CST method was extended by Zhu et al. [19] to produce the intuitive Class Shape Transformation (iCST) approach. The iCST approach has been successfully applied to the parameterisation of various aero-engine aerodynamic shapes such as intakes [25], nacelles [26–29] and separate-jet exhaust nozzles [4,30,31]. While methods for the generation of axisymmetric aero-engines

* Corresponding author.
E-mail address: jjotter26@gmail.com (J.J. Otter).

https://doi.org/10.1016/j.ast.2019.05.038
1270-9638/© 2019 Rolls-Royce plc. Published by Elsevier Masson SAS. This is an open access article under the CC BY license (http://creativecommons.org/licenses/by/4.0/).

Nomenclature

Roman symbols

$\hat{\mathbf{e}}_x, \hat{\mathbf{e}}_r, \hat{\mathbf{e}}_\psi$	Cylindrical unit vectors	
dA	Infinitesimal surface element parallel to surface	m^2
dS	Infinitesimal surface element normal to surface	m^2
V	Velocity vector	$m\,s^{-1}$
$\dot{m}$	Mass flow rate	$kg\,s^{-1}$
ϕ_{nac*}	Modified nacelle drag	N
A_r	iCST shape function coefficients	
$C(\overline{\psi})$	iCST class function	
C_{V*}	Modified velocity coefficient	
F_G	Gauge stream force	N
$H(\overline{\psi})$, $\Theta(\overline{\psi})$, $E(\overline{\psi})$	iCST analytical spatial functions	
$K_{r,n}$	Binomial coefficients	
n	Order of a curve or system	
$N^i_{\overline{\psi}}$	Number of control points for the ith distribution	
N_d	Number of distributions	
NPF_c	Corrected net propulsive force	N
p	Static pressure	Pa
q_{inf}	Freestream dynamic pressure	Pa
$S(\overline{\psi})$	iCST shape function	
V^{Ideal}	Fully expanded isentropic nozzle velocity	$m\,s^{-1}$
x, r, ψ	Cylindrical co-ordinates	m, m, degrees

Greek symbols

$\overline{\psi}$	Non-dimensional azimuthal angle	
ϕ	Force in the drag domain	N
ρ	Density	$kg\,m^{-3}$
τ	Local shear stress	N
θ	Force in the thrust domain	N
υ	A generic geometric parameter	
υ_{offset}	iCST offset normal to the abscissa	
Υ_j	Azimuthal control points	

exhaust nozzles have been successfully developed [4,30,31], these CST based methods have not previously been extended for the design of non-axisymmetric exhaust nozzle configurations.

Although research has been conducted into the effects of non-axisymmetric exhaust geometries on noise propagation and jet mixing, the current literature does not adequately address how exhaust system performance may be altered by the introduction of non-axisymmetric design features. The primary aim of this work is to establish an iCST based design methodology for non-axisymmetric separate-jet exhaust nozzles. In order to achieve this aim, two novel contributions to the field of aero-engine exhaust system design are presented. Firstly, the development of an iCST based fully parametric, intuitive and analytical approach to the design of non-axisymmetric separate-jet exhaust systems. Secondly, the evaluation of aerodynamic performance of non-axisymmetric exhaust system design features for high BPR aero-engine architectures.

2. Methodology

The methodology of this paper is split into three main components: the generation of non-axisymmetric engine geometries (Section 2.1), the production of suitable computational meshes (Section 2.3) and the evaluation of the engine and nozzle aerodynamic performance metrics (Section 2.2).

2.1. Geometry generation

2.1.1. Overview

An aero-engine geometry can be represented by a set of two-dimensional aerolines which are defined in a cylindrical co-ordinate system ($x\hat{\mathbf{e}}_x$, $r\hat{\mathbf{e}}_r$, $\psi\hat{\mathbf{e}}_\psi$). These aerolines can be split into three sets which correspond to the engine intake, nacelle and exhaust system (Fig. 1). The set of design variables which are used to define the intake, nacelle and exhaust aerolines in this two-dimensional representation are reported by Christie [25], Heidebrecht [26] and Goulos et al. [4] respectively. The geometry generation method outlined in this work creates non-axisymmetric geometries through an extension of the two-dimensional approaches. A three-dimensional geometry is generated by constructing multiple two-dimensional aerolines in the $\hat{\mathbf{e}}_x - \hat{\mathbf{e}}_r$ plane at multiple azimuthal angles (ψ).

To construct multiple aerolines around the azimuth each design variable must be specified as a function of ψ. Previous studies into non-axisymmetric exhaust nozzles predominantly incorporate azimuthal variations through the elliptical variation of trailing edge radii [12,13]. Within this work the azimuthal variation of every design parameter is controlled with iCST curves. The method allows for a much larger range of geometries to be created as there is no requirement to follow an elliptical variation. A particular strength is that this increased freedom does not come at a cost of sacrificing an analytical formulation, which ensures a deterministic relationship between the input variables and resultant geometric outputs.

The geometry generation process developed within this paper firstly defines how each design parameter varies with the azimuthal angle (ψ). iCST curves are generated for each geometric design variable as a function of the azimuthal angle ψ. With each nozzle annuli defined, the bypass and core nozzle geometric exit areas are calculated with the rolling ball method [32]. Each nozzle exit geometric area is adjusted iteratively through variations of the axial and radial positions of either the inner or outer nozzle annuli until the desired geometric exit area is met. With each of the design variables specified as a function of ψ and the exit annuli sized correctly, iCST curves for each aeroline in the local $\hat{\mathbf{e}}_x - \hat{\mathbf{e}}_r$ plane are constructed (Fig. 1).

2.1.2. Azimuthal variation of design variables

In order to define multiple aerolines around the azimuth, all of the design variables which are required to define an aeroline in the corresponding $\hat{\mathbf{e}}_x - \hat{\mathbf{e}}_r$ plane must be specified as a function of ψ. Example of such variables include the radii which define each nozzle annulus ($r^{out}_{BP-exit}$, $r^{in}_{BP-exit}$, $r^{out}_{CR-exit}$, $r^{in}_{CR-exit}$ denoted in Fig. 1). The azimuthal variation of each variable is treated in the same manner and as such this section considers a generic design variable (υ) which is to be defined around the engine annulus i.e. between ψ of 0° and 360°. The general form of an iCST function ($\upsilon(\overline{\psi})$) over the normalised space $\overline{\psi} \in (0, 1)$ is given in Eq. (1).

$$\upsilon(\overline{\psi}) = C(\overline{\psi})S(\overline{\psi}) + \overline{\psi}\upsilon_{offset} \tag{1}$$

The symbol $C(\overline{\psi})$ denotes the class function, $S(\overline{\psi})$ denotes the shape function (which is a nth order Bernstein polynomial defined in Eq. (2)) and υ_{offset} is an offset normal to the abscissa [4]. The class function can take different functional forms depending on the application. However, within this work a class function of unity was used ($C(\overline{\psi}) = 1$) such that, in conjunction with a shape function of unity, a uniform azimuthal distribution would be produced.

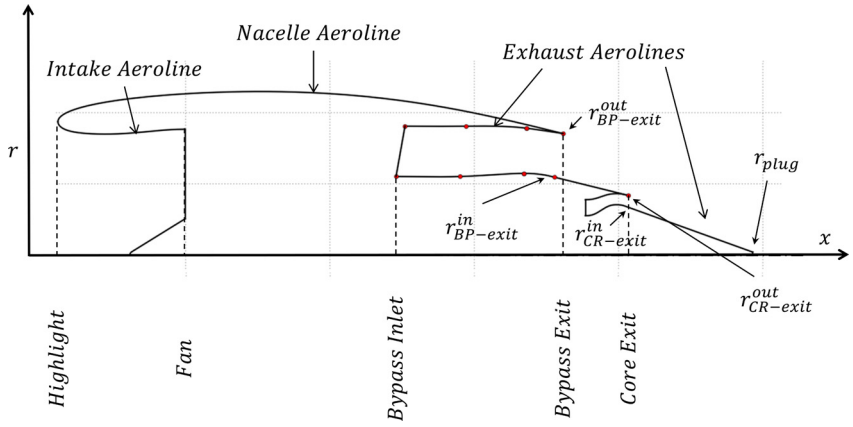


Fig. 1. Aerolines in the $\hat{\mathbf{e}}_x - \hat{\mathbf{e}}_r$ plane.

$$S(\overline{\psi}) = \sum_{r=0}^{n} \{A_r K_{r,n} \overline{\psi}^r (1-\overline{\psi})^{n-r}\} \tag{2}$$

$$K_{r,n} = \frac{n!}{r!(n-r)!} \tag{3}$$

The symbol $K_{r,n}$ denotes the binomial coefficients (Eq. (3)) and A_r denotes weighting factors which are applied to the rth binomial coefficient. With a class function of unity the shape function along with its first and second derivatives can be expressed by Eq. (4), (5) and (6) [4] where $H_{r,n}(\overline{\psi})$, $\Theta_{r,n}(\overline{\psi})$ and $E_{r,n}(\overline{\psi})$ are defined in Eq. (7), (8) and (9) [4].

$$\upsilon(\overline{\psi}) = \sum_{r=0}^{n} \{A_r K_{r,n} H_{r,n}(\overline{\psi})\} + \overline{\psi}\upsilon_{offset} \tag{4}$$

$$\upsilon(\overline{\psi})' = \sum_{r=0}^{n} \{A_r K_{r,n} \Theta_{r,n}(\overline{\psi})\} \tag{5}$$

$$\upsilon(\overline{\psi})'' = \sum_{r=0}^{n} \{A_r K_{r,n} E_{r,n}(\overline{\psi})\} \tag{6}$$

$$H_{r,n}(\overline{\psi}) = \overline{\psi}^r (1-\overline{\psi})^{n-r} \tag{7}$$

$$\Theta_{r,n}(\overline{\psi}) = r(\overline{\psi}^{r-1})(1-\overline{\psi})^{n-r} - \overline{\psi}^r (n-r)(1-\overline{\psi})^{n-r-1} \tag{8}$$

$$E_{r,n}(\overline{\psi}) = r(r-1)\overline{\psi}^{r-2}(1-\overline{\psi})^{n-r} - 2r\overline{\psi}^{r-1}(n-r)(1-\overline{\psi})^{n-r-1} + \overline{\psi}^r (n-r)(n-r-1)(1-\overline{\psi})^{n-r-2} \tag{9}$$

To define $\upsilon(\overline{\psi})$ a set of boundary conditions must be specified over the normalised $\overline{\psi}$ space. The Bernstein polynomial weights, $A_r, r = 1, ..., r = n-1$, can be calculated based on these boundary conditions. The weights are calculated through the solution of a $(n-1)$ by $(n-1)$ system of linear equations derived from Eq. (4), (5) and (6). The order of the system is determined by the number of boundary conditions defined. The resultant weighting coefficients uniquely satisfy the imposed boundary conditions.

A boundary condition, herein referred to as a control point and denoted with the symbol Υ, must specify υ, or one of its derivatives, at a given value of $\overline{\psi}$. For example, $\Upsilon(0) = 1$ denotes that the resultant iCST curve for υ must have a value of 1 at $\overline{\psi} = 0$. The distribution of $\upsilon(\overline{\psi})$ is controlled by five parameters: N, the number of control points over the normalised $\overline{\psi}$ space; $\overline{\psi}_j$, the location of the jth control point along the $\overline{\psi}$ axis; Υ_j, the value of the geometric parameter at $\overline{\psi}_j$; Υ'_j, the gradient at $\overline{\psi}_j$ and Υ''_j, the second derivative at $\overline{\psi}_j$. At each control point any combination of Υ_j, Υ'_j and Υ''_j can be defined. To ensure positional, gradient and curvature continuity around the annulus, the values of Υ, Υ' and Υ'', respectively, must be equal at the 0th and Nth control points.

As the number of control points used to define υ increases, so to does the order of the resultant iCST distribution [25,26]. Although such a high order iCST may be necessary to meet a given set of constraints, it may lead to oscillatory behaviour in υ, υ', υ'' and hence curvature $\left(\frac{\upsilon''}{(1+\upsilon'^2)^{1.5}}\right)$. From an aerodynamic design viewpoint, it is essential that the curvature of a geometric entity is easily controlled through the parametric geometry generation method. This is of paramount importance in regions that are subject to transonic flow, as variations in curvature can lead to unnecessary flow accelerations and various associated loss mechanisms. Furthermore, with the existing formulation of the proposed method it is not possible to localise variations in υ, i.e. changes in the any of Bernstein coefficients $(A_r, r = 1, ..., r = n-1)$ will lead to variations in υ throughout the normalised $\overline{\psi}$ space.

These issues can be alleviated through the division of υ into N_d separate iCST curves over the normalised $\overline{\psi}$ space (Eq. (10)). Where N_d is the number of iCST distributions which υ is to be split into. This split allows regions of the normalised $\overline{\psi}$ space to be controlled independently of one another. To ensure continuity up to the second derivative (υ'') the following conditions are placed on the control points: $\Upsilon_i(\overline{\psi}_i) = \Upsilon_{i-1}(\overline{\psi}_i)$, $\Upsilon'_i(\overline{\psi}_i) = \Upsilon'_{i-1}(\overline{\psi}_i)$ and $\Upsilon''_i(\overline{\psi}_i) = \Upsilon''_{i-1}(\overline{\psi}_i)$ where i refers to the ith iCST distribution.

$$\upsilon(\overline{\psi}) = \begin{cases} \upsilon_0(\overline{\psi}) \text{ for } 0 < \overline{\psi} < \overline{\psi}_0 \\ \upsilon_1(\overline{\psi}) \text{ for } \overline{\psi}_0 < \overline{\psi} < \overline{\psi}_1 \\ ... \\ \upsilon_i(\overline{\psi}) \text{ for } \overline{\psi}_{i-1} < \overline{\psi} < \overline{\psi}_i \end{cases} \tag{10}$$

To illustrate the benefits of splitting the distribution of υ consider an example where the desired azimuthal distribution of υ is to be split into three distinct sections (Fig. 2). Section 1 ranges from $\overline{\psi} = 0$ to $\overline{\psi} = 0.33$ and has a peak υ value of 0.33 at $\overline{\psi} = 0.167$. Section 2 ranges from $\overline{\psi} = 0.33$ to $\overline{\psi} = 0.66$ and is to have a constant value of υ. Section 3 is to vary from $\overline{\psi} = 0.66$ to $\overline{\psi} = 1$ and is to have a minimum υ value of 0.5 at $\overline{\psi} = 0.767$. The first and second derivatives of υ with respect to $\overline{\psi}$ are required to be zero at $\overline{\psi} = 0$, 0.33, 0.66 and 1.0. For this example over the region of $\overline{\psi}$ from 0 to 1 a total of 14 control points are required (shown as circles in Fig. 2): 6 in Υ, 4 in Υ' and 4 in Υ''. An iCST distribution for υ to match these constraints can be created with a single high order iCST curve between $\overline{\psi}$ or by splitting into multiple lower order iCST curves.

To meet the constraints of this example with a single iCST, a 13th order curve is required. With a single iCST it is not possible to maintain a constant value of υ across the region of $0.33 < \overline{\psi} <$

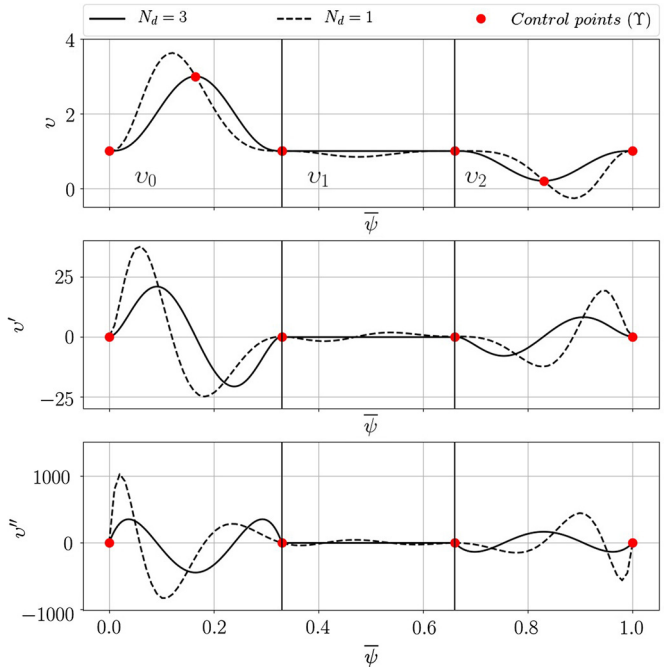


Fig. 2. Example split iCST curve.

0.66 as an inflection point is introduced at $\overline{\psi} = 0.5$ (dotted line in Fig. 2). In addition, the peak value requirements of υ in the region of $0 < \overline{\psi} < 0.33$ and the minimum value of υ in the region of $0.66 < \overline{\psi} < 1$ have not been met. This example highlights how a high order iCST curve leads to oscillatory values of υ and its derivatives. If the variation of υ is split (as outlined in Equation 10) into three distributions ($N_d = 3$), $\overline{\psi}_0 = 0.33$, $\overline{\psi}_1 = 0.66$, $\overline{\psi}_2 = 1.0$ then the desired variation of υ can be achieved (solid line in Fig. 2). As a result of the split iCST υ_0 is an 6th order iCST curve, υ_1 is a linear iCST curve with zero curvature and υ_2 is an 6th order iCST curve (Fig. 2).

In contrast to a single iCST, the derivatives of υ produced by a split iCST method are no longer mathematically smooth over the normalised $\overline{\psi}$ space. However, the derivative to which a continuous function is produced is set by the highest derivative of the control point at the boundary of each distribution, which in this example was υ''. The ability to split the azimuthal variation into multiple distributions is desirable mathematically as it can prevent the oscillatory behaviour associated with high order polynomial curves and it is also desirable aerodynamically as it provides greater control of curvature over the normalised $\overline{\psi}$ space. In summary, the parameters that are used to control the azimuthal distribution of υ are:

- N_d – The number of distributions into which the variation of υ will be split into.
- N_i – The number of control points defined for the ith distribution
- Υ^i_j – The jth value of the imposed generic design variable in the ith distribution
- $\Upsilon^{i\prime}_j$ – The imposed gradient of the jth generic design variable in the ith distribution
- $\Upsilon^{i\prime\prime}_j$ – The imposed second derivative of the jth generic design variable in the ith distribution

2.2. Thrust and drag bookkeeping

The thrust and drag bookkeeping method and engine station numbering system (Fig. 3) presented are based on well-established methods [33]. Each wall force is calculated from a CFD solution through the integration of pressure and shear terms (Eq. (11)). Moreover, each force can also be resolved into the drag direction which is aligned with the freestream flow (denoted with $\hat{\mathbf{e}}_D$ in Fig. 3). In addition to the wall forces, it is necessary to calculate the gauge stream forces (F_G given by Eq. (12)) at various engine stations.

$$\phi^x, \theta^x = \iint_{surface} ((p - p_{atm})\hat{\mathbf{e}}_x \cdot \mathbf{dS} + \iint_{surface} \tau \hat{\mathbf{e}}_x \cdot \mathbf{dA} \tag{11}$$

$$F^x_G = \iint_{Area} (\rho\,|\mathbf{V}|\,\mathbf{V} \cdot \hat{\mathbf{e}}_x + (p - p_{atm}))\mathbf{dS} \cdot \hat{\mathbf{e}}_x \tag{12}$$

At typical cruise conditions, the engine net propulsive force (NPF^D defined in Eq. (13) where the superscript D denotes that the force has been resolved into the $\hat{\mathbf{e}}_D$ direction) serves as a metric for the overall aerodynamic performance of an aero-engine. The NPF^D can be broken down into the modified gross propulsive force (GPF^D_* Eq. (14)), which accounts for the thrust domain, and the (ϕ^D_{nac*} Eq. (15)) which accounts for the drag domain. The term ϕ^D_{nac*} has been evaluated with the modified near field method [34].

$$NPF^D = GPF^D_* - F^D_{G0} - \phi^D_{nac*} \tag{13}$$

$$GPF^D_* = F^D_{G19} + F^D_{G9} + \theta^D_{cc} + \theta^D_{plug} \tag{14}$$

$$\phi^D_{nac*} = \phi^D_{pre} + \phi^D_{cowl} \tag{15}$$

A quantitative measure for the aerodynamic performance of an exhaust system is provided by the velocity coefficient. The modified velocity coefficient (C^D_{V*} Eq. (16)) is defined as the ratio of the actual gross propulsive force generated from the exhaust system to the thrust which would result from the fully-expanded jet velocities (V_{ideal} defined in [4]) and the mass flow rates derived from the CFD calculation.

$$C^D_{V*} = \frac{GPF^D_*}{\dot{m}_7 V^{ideal}_9 + \dot{m}_{13} V^{ideal}_{13}} \tag{16}$$

For a given exhaust system design, the mass flow rates which are discharged through the bypass and core nozzles are a direct result of the CFD analysis and hence are not known *a priori*. As a result of this mass flow rate imbalance ($\dot{m}_2 \neq \dot{m}_7 + \dot{m}_{13}$) the engine NPF computed based strictly on CFD results is no longer a valid measure of engine performance. Within this context, corrected gross and net propulsive forces have been defined (GPF^D_{*c} and NPF^D_c defined in Eqs. (17) and (18) respectively). The values of bypass and core mass flow rates chosen ($\dot{m}^{Cycle}_7$ and $\dot{m}^{Cycle}_{13}$) were determined from the engine thermodynamic cycle analysis. This method works under the assumption that any changes to C^D_{V*} and ϕ^D_{nac*} due to the discrepancy between the CFD and cycle bypass and core nozzle mass flow rates are negligible.

$$GPF^D_{*c} = C^D_{V*}(\dot{m}^{Cycle}_7 V^{ideal}_7 + \dot{m}^{Cycle}_{13} V^{ideal}_{13}) \tag{17}$$

$$NPF^D_c = GPF^D_{*c} - F^D_{G0} - \phi^D_{nac*} \tag{18}$$

2.3. Computational fluid dynamic method

The aerodynamic performance of an engine geometry is assessed through the use of Computational Fluid Dynamics (CFD). Thus approach has been validated against experimental data by Otter et al. [35]. An implicit density based compressible solver [36] with second order upwind spatial discretisation scheme was used for solve the governing conservation equations. The $k - \omega$ Shear Stress Transport (SST) [37] model was implemented to close the

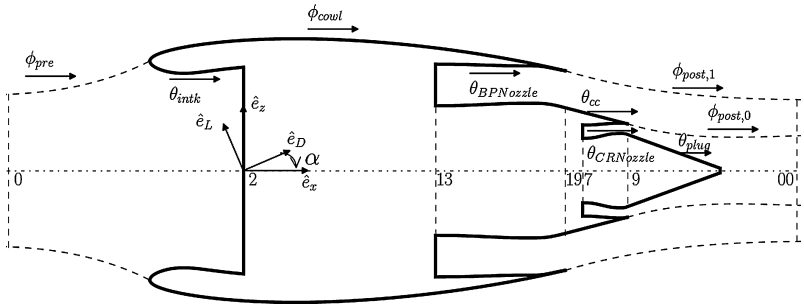
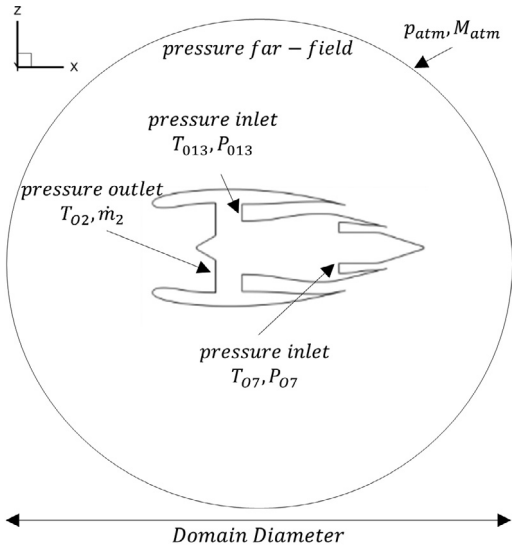
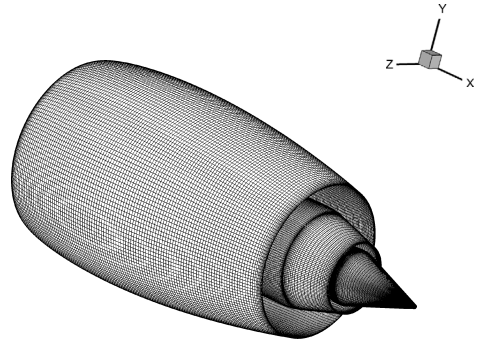


Fig. 3. Schematic for the breakdown of Thrust and Drag.



(a) Schematic of Computational Domain



(b) Close-up of surface mesh

Fig. 4. Computational domain and surface mesh.

system of equations. The initial cell height normal to each viscous wall surface was set to ensure that the non-dimensional wall distance was less than one and hence wall functions were not used. The ideal gas law was used as the equation of state for the working fluid and an eighth order polynomial expression was used to model the specific heat capacity as a function of static temperature [38]. Sutherland's law was used to calculate dynamic viscosity [39].

The computational domain (Fig. 4a) featured a spherical pressure far-field boundary condition to model freestream conditions. A pressure outlet boundary condition was used to model the fan face and pressure inlets were used to model the bypass and core nozzle inlets. Total temperature and total pressure were specified on each pressure outlet and inlet face. Based on the exhaust nozzle modelling guidelines outlined by the AIAA Propulsion Aerodynamics Workshop [40], a turbulent intensity of 5% and turbulent viscosity ratio of 1 was applied at the inlet of both the fan and core streams. A static pressure boundary was used at fan face pressure-outlet to achieve a given fan mass flow rate. Each engine aeroline was modelled as a viscous adiabatic wall. To quantify the effect of the computational domain on the nozzle performance metrics three different diameters for the spherical domain were investigated. Domains diameters of 60D, 80D, and 100D were chosen where D was the maximum diameter of the engine nacelle. At a freestream Mach number of 0.85 a decrease of 0.01% in $C^D_{V_*}$ (Eq. (13)) was observed between the 60D and 80D domains. Between the 80D and 100D the decrease in $C^D_{V_*}$ was 0.005%. Similarly, values of 0.56% and 0.27% were found for the ϕ^D_{nac*}. As a result the 100D domain size was used for all of the computations in this study.

Each engine configuration was meshed with a fully structured multi-block approach [41]. The resultant mesh consisted of 11 million hexahedral elements with an example surface mesh shown in Fig. 4b. A total of three mesh resolutions with a domain size of 100D were investigated such that grid independence could be assessed through the calculation of a Grid Convergence Index (GCI) [42,43]. The first cell height remained fixed across all the meshes investigated. The element count for the coarse, medium and fine meshes was 6.3 million, 8.2 million and 11.2 million respectively. The GCI for $C^D_{V_*}$ and ϕ^D_{nac*} were found to be 0.02% and 0.3% respectively. All of the computations presented within this work are based on the mesh sizing from the fine mesh (11.2 million elements) as, for the metrics of interest, it has displayed monotonic behaviour with mesh refinement and lead to small values of GCIs.

3. Results and discussion

The configurations presented within this section were designed to have a BPR above 15, to cruise at a freestream Mach number of 0.85 with a rated cruise standard net thrust of approximately 60 kN. The bypass nozzle operated with a pressure ratio of 2.2 and the core nozzle with a pressure ratio of 1.6. Two example design cases have been investigated (Table 1). Case A represents a design where, due to installation requirements, the topline value of $r^{out}_{BP-exit}$ ($\psi = 0°$) has to be reduced in order to achieve a required local clearance between the engine and airframe. Case B represents an elliptical type design whereby both the top and bottom line $r^{out}_{BP-exit}$ ($\psi = 0°$ and $\psi = 180°$) have been reduced relative to the sideline ($\psi = 90°$). Such an elliptical style case may be considered in an attempt to reduce jet noise [12,13]. For Case A, azimuthal variation of $r^{out}_{BP-exit}$ was controlled by the value of $r^{out}_{BP-exit}$ at $\psi = 0°$. For Case B azimuthal variation of $r^{out}_{BP-exit}$ was controlled by values of $r^{out}_{BP-exit}$ at $\psi = 0°$ and $\psi = 180°$. For both cases the value of $r^{out}_{BP-exit}$ at $\psi = 0°$ and $\psi = 180°$ where varied as a ratio of the value of $r^{out}_{BP-exit}$ at $\psi = 90°$ (Table 1). This radius ratio ($\frac{r}{r(\psi=90°)}$) was varied between 0.95 and 1.025.

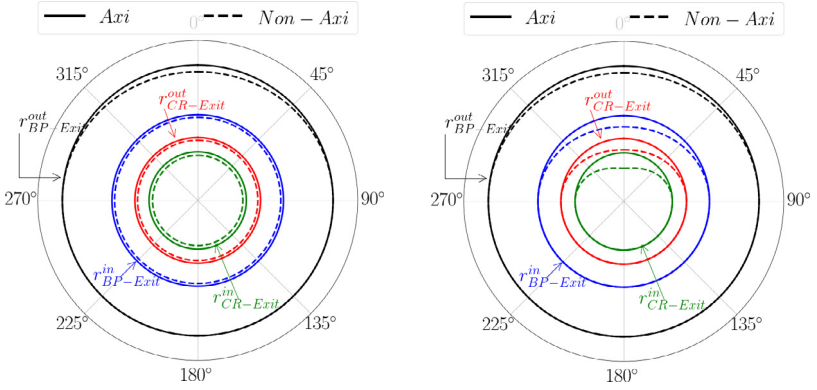
Table 1
Matrix of bypass nozzles designs investigated.

Case	Radius ratio $\frac{r^{out}_{BP-exit}(\psi=0°)}{r^{out}_{BP-exit}(\psi=90°)}$	Radius ratio $\frac{r^{out}_{BP-exit}(\psi=180°)}{r^{out}_{BP-exit}(\psi=90°)}$
A	0.95, 0.975, 1, 1.025	1
B	0.95, 0.975, 1, 1.025	0.95, 0.975, 1.0, 1.025

3.1. Engine geometries

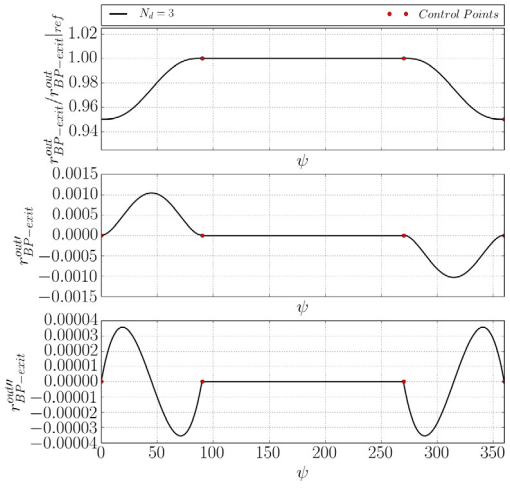
For Case A there should not be any variation in $r^{out}_{BP-exit}$ between $\psi = 90°$ to 270° (Fig. 5a). In order to prevent such variations between $\psi = 90°$ to 270° three iCST distributions were used to control $r^{out}_{BP-exit}$ (Fig. 5c). The first distribution controlled the region from $\psi = 0°$ to 90°, the second controlled the region of zero curvature from $\psi = 90°$ to 270° and the final distribution from $\psi = 270°$ to 360°. To define these distributions four constraints were specified in each of $r^{out}_{BP-exit}$, $r^{out\prime}_{BP-exit}$ and $r^{out\prime\prime}_{BP-exit}$ at $\psi = 0°$, $\psi = 90°$, $\psi = 270°$ and $\psi = 360°$ (Fig. 5c). Note that the constraints placed at $\psi = 360°$ are included to ensure continuity of $r^{out}_{BP-exit}$, $r^{out\prime}_{BP-exit}$ and $r^{out\prime\prime}_{BP-exit}$. As a result of these constraints, the first and third distributions formed 5th order iCST curves. Without the division into three separate iCST distributions it would not be possible to ensure zero curvatures between $\psi = 90°$ and $\psi = 180°$.

With the azimuthal variation of $r^{out}_{BP-exit}$ specified the separate-jet exhaust system can now be designed. The developed methodology is sufficiently flexible to enable two methods for afterbody design to be employed. For the first method the afterbody exit annuli are circular (Fig. 5a) with each radius scaled in order to achieve the desired nozzle exit flow area. In contrast, the afterbody exit annuli for the second method follow a scaled non-circular distribution based on $r^{out}_{BP-exit}$ (Fig. 5b). The full afterbody design process is outlined hereafter: firstly, the azimuthal distribution of $r^{out}_{BP-exit}$ is specified, after which $r^{in}_{BP-exit}$ (circular or non-circular) was varied iteratively until the desired bypass nozzle exit area was met. The core nozzle outer radius ($r^{out}_{CR-exit}$) was set based on the conical core cowl angle and core cowl length (as defined in [4]). For all designs within this paper the core cowl angle and length were kept constant around the azimuth and hence $r^{out}_{CR-exit}$ followed the same azimuthal variation as $r^{in}_{BP-exit}$. Finally, the value of the core nozzle inner radius ($r^{in}_{CR-exit}$) was iterated upon until the target core nozzle area was met. For the circular afterbody case, there was a reduction in $r^{in}_{BP-exit}$, and hence $r^{out}_{CR-exit}$, relative to the axisymmetric case in order to match the bypass nozzle exit area requirement (Fig. 5a). Furthermore, $r^{in}_{CR-exit}$ was also reduced in order to meet the target core nozzle exit area (Fig. 5a). For the non-circular afterbody design there is no circumferential variation of any radii between $\psi = 90°$ and 270° as the nozzle area requirements were met through radial variations between $\psi = 270°$ and 90° (Fig. 5b).



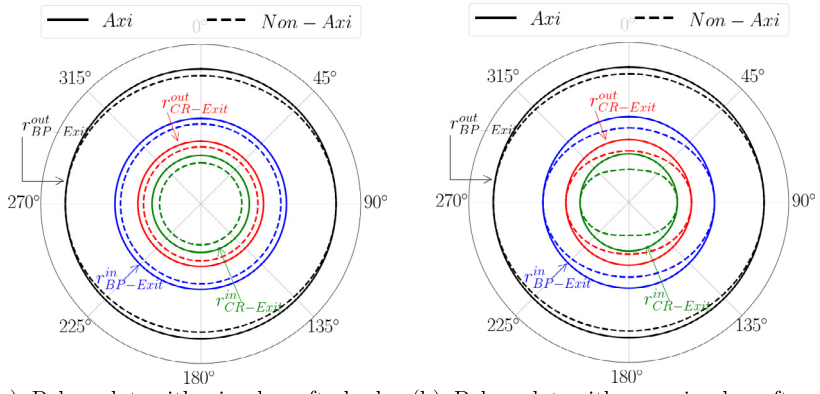
(a) Polar plot with circular afterbody with radius ratio of 0.95

(b) Polar plot with non-circular afterbody with radius ratio of 0.95



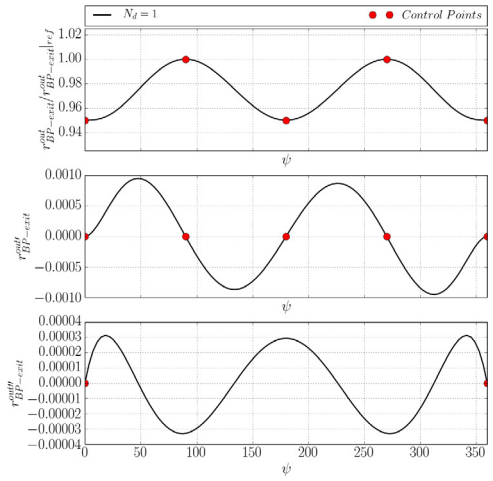
(c) Constraints and Azimuthal variation of $r^{out}_{BP-exit}$ and its derivatives with a radius ratio of 0.95

Fig. 5. Geometry definition for case A.



(a) Polar plot with circular afterbody with radius ratio of 0.95

(b) Polar plot with non-circular afterbody with radius ratio of 0.95



(c) Constraints and Azimuthal variation of $r^{out}_{BP-exit}$ and its derivatives with a radius ratio of 0.95

Fig. 6. Geometry definition for case B.

For Case B the requirement to have regions of zero azimuthal curvature has been relaxed to demonstrate the choices available to an aerodynamic designer. A single iCST was used to control $r^{out}_{BP-exit}$ from $\psi = 0°$ to 360°. A total of five constraints were applied to each of $r^{out}_{BP-exit}$ and $r^{out\prime}_{BP-exit}$ at $\psi = 0°$, $\psi = 90°$, $\psi = 180°$, $\psi = 270°$ and $\psi = 360°$ (Fig. 6c). Furthermore, two constraints were applied in $r^{out\prime\prime}_{BP-exit}$ at $\psi = 0°$ and $\psi = 360°$ (Fig. 6c) and as a result an 11th order iCST curve was produced. As was the case with case A two different methods for afterbody design were applied and can be seen in Figs. 6a and 6b for a radius ratio of 0.95. Due to the reduced value of $r^{out}_{BP-exit}$ around the annulus, a substantial change in $r^{in}_{BP-exit}$, $r^{out}_{CR-exit}$ and $r^{in}_{CR-exit}$ can be observed relative to the axisymmetric case in order to meet the nozzle exit area requirements (Fig. 6a). For the non-circular afterbody design, $r^{in}_{BP-exit}$, $r^{out}_{CR-exit}$ and $r^{in}_{CR-exit}$ were set to follow the same azimuthal variation in radius as $r^{out}_{BP-exit}$. Overall, these sample cases illustrate a potential design requirement for a non-axisymmetric exhaust system and are appropriate examples to highlight the capability of the current method.

3.2. The effect of non-axisymmetric nozzle design on net propulsive force

In order to represent a typical cruise flight condition, each case was computed with a freestream Mach number of 0.85 at a typical engine cruise incidence (α defined in Fig. 3) of 3 degrees. Quantification of the impact of each design on the aerodynamic performance of the engine is provided by a percentage change (Δ) relative to the axisymmetric baseline (Fig. 7). The most important metric is the corrected net propulsive force (NPF^D_c defined in Eq. (18)) as this accounts for the aerodynamic performance in both the thrust and drag domains. Note that changes in modified nacelle drag (ϕ^D_{nac*} defined in Eq. (15)) and corrected gross propulsive force (GPF^D_{*c} defined in Eq. (17)) are reported as percentage values of the axisymmetric NPF^D_c such that they are in a common currency. In order to contextualise the subsequent results it should be noted that an increase of 0.1% in net propulsive force approximately equates to reduction of 0.1% in SFC.

Furthermore, the aim of this work is to demonstrate the method for the design of general non-axisymmetric exhausts. This could be to accommodate other installation requirements such as physical size, wing-pylon clearance and engine mounting systems. Therefore, the immediate effect on the exhaust system performance and NPF^D_c may not be the dominant term in overall system. For example, the work of Daggett [44] highlighted the complex, multi-disciplinary nature of some aspects of propulsion integration. Within this context, it is useful to have a design method that can facilitate non-axisymmetric exhaust systems. Similarly, within the context of the overall system performance, it is useful to understand the aerodynamic changes, either positive or negative, that can arise from potentially necessary non-axisymmetric requirements associated with the installation of the aero-engine.

For case A a reduction in $r^{out}_{BP-exit}$ at $\psi = 0°$ was detrimental to NPF^D_c relative to the axisymmetric case (Fig. 7a). The afterbody

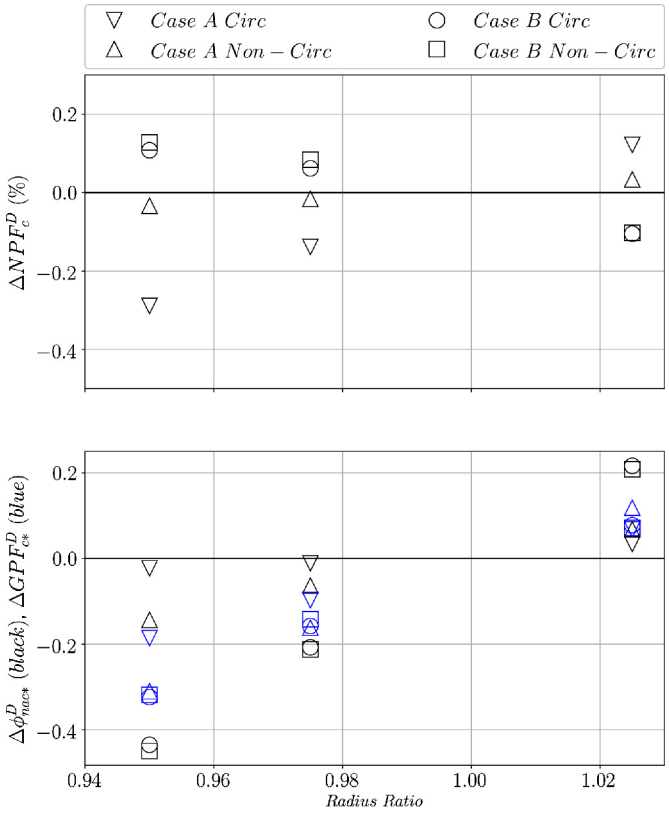


Fig. 7. Variation of NPF_c^D (a), ϕ^D_{nac*} (b) and GPF^D_{*c} (b) with $r^{out}_{BP-exit}$ $\psi = 0°$ and $r^{out}_{BP-exit}$ $\psi = 180°$.

design approach has a large impact on this reduction in NPF_c^D. For example, at a radius ratio of 0.95 the non-circular afterbody design reduced NPF_c^D by 0.03% compared to the circular case which has a 0.26% reduction in NPF_c^D. From this it can be concluded that if $r^{out}_{BP-exit}$ is to be reduced at $\psi = 0°$, then to minimise losses in NPF_c^D, a non-circular afterbody design approach should also be employed. For a radius ratio of 0.95 both afterbody design cases from Case A are detrimental in terms of nozzle performance, as shown by negative values ΔGPF^D_{*c} (Fig. 7b). Conversely, a benefit to nacelle performance is observed at a radius ratio of 0.95, as shown by a reduction of ϕ^D_{nac*} and hence negative values of $\Delta\phi^D_{nac*}$ (Fig. 7b). However, ΔNPF_c^D is negative for both of these designs as the beneficial reduction in modified nacelle drag is outweighed by the penalising decrease in nozzle performance.

At a radius ratio of 1.025 ΔNPF_c^D is positive for both afterbody design methodologies from Case A (Fig. 7a). However, with a radius ratio of greater than one the circular afterbody design was shown to be favourable in terms of NPF_c^D, a change relative to the axisymmetric design of 0.11% compared to 0.03% was found (Fig. 7a). This increase in NPF_c^D arises due to a positive ΔGPF^D_{*c} (Fig. 7b) for a relatively small increase in ϕ^D_{nac*} (Fig. 7b).

For the designs of case B the opposite trend in terms of radius ratio and NPF_c^D was observed. For example, with a radius ratio of less than 1 an increase in NPF_c^D occurs and at radius ratios greater than one a decrease in NPF_c^D occurs. For example, at a radius ratio of 0.95 an increase of 0.12% and 0.10% was found for the non-circular and circular afterbody designs respectively. This increased NPF_c^D arises as, compared to Case A, the Case B design displays a larger reduction in drag $\Delta\phi^D_{nac*}$ (−0.42% compared to −0.15%), whilst the penalty to nozzle performance remains roughly constant (ΔGPF^D_{*c} values of −0.31%). In other words, for a constant nozzle performance the nacelle performance has improved. However, at a radius ratio of 1.025, NPF_c^D reduced by 0.09% for both the circular and non-circular afterbody designs respectively. This demonstrates how for NPF_c^D cases B were relatively insensitive to afterbody design compared with case A.

Table 2
Summary of best performing non-axisymmetric designs.

Case	Radius ratio	Afterbody type	ΔNPF_c^D(%)
B	0.95	Non-circ	0.13
A	1.025	Circ	0.12
B	0.95	Circ	0.11

From the two case studies investigated in this section it has been shown that at typical cruise flight conditions non-axisymmetric bypass nozzles can lead to variations of NPF_c^D between 0.13% and −0.28%. If the trailing edge of the nacelle topline ($r^{out}_{BP-exit}(\psi = 0°)$) is required to be smaller that the sideline radius ($r^{out}_{BP-exit}(\psi = 90°)$) then a non-circular afterbody design should be employed to minimise losses to NPF_c^D. Conversely, if the aforementioned topline radius is to be greater than one then a circular afterbody design should be implemented to improve NPF_c^D relative to axisymmetric case. Furthermore, a reduction of $r^{out}_{BP-exit}$ at $\psi = 0°$ and $\psi = 180°$ was shown to be beneficial to NPF_c^D owing to a reduction in the modified nacelle drag (ϕ^D_{nac*}) by 0.4%. The designs from the above study which showed the greatest improvement to NPF_c^D are summarised in Table 2. These results indicate that if, for mechanical reasons, $r^{out}_{BP-exit}$ is required to be reduced at the topline then the bottomline radius should also be modified reduced in order to maximise the engine NPF_c^D (following the design of Case B). If the value of $r^{out}_{BP-exit}$ at the topline is required to be larger, then the bottomline radius should remain fixed and circular afterbody should be employed (following the design of Case A).

3.3. The effect of non-axisymmetric nozzle design on modified nacelle drag

The results from the previous section demonstrated that a reduction of both the top and bottom line nacelle trailing edge radius (as per Fig. 6a) led to an increase in of NPF_c^D up to 0.12% relative to an axisymmetric engine. The main cause of this increase in NPF_c^D was due to a reduction in modified nacelle drag (ϕ^D_{nac*}). This drag reduction can be visualised through the evaluation of the local surface force coefficient resolved in the drag direction ($\frac{\phi^D_{local}}{q_{inf}}$, Eq. (19))

$$\frac{\phi^D_{local}}{q_{inf}} = ((p - p_{atm})\hat{\mathbf{e}}_D \cdot \hat{\mathbf{dS}} + \tau\hat{\mathbf{e}}_D \cdot \hat{\mathbf{dA}} \tag{19}$$

Before examining the local surface force distributions, the static pressure coefficient (C_p) around the azimuth of the axisymmetric nacelle at an incidence of 3° should be considered (Fig. 8). Due to the incident flow onto the nacelle, a greater amount of suction is observed at the topline ($\psi = 0°$) of the nacelle compared to the bottomline ($\psi = 180°$), with peak C_p values of −0.8 and −0.4 respectively. At axial locations downstream of 0.2 x/L_{nac} the static pressure coefficient can be seen to increase around the azimuth. Moreover, azimuthal variations in static pressure further downstream of 0.5 x/L_{nac} can be seen to reduce (Fig. 8). At the trailing edge of the nacelle a uniform C_p value of 0.2 is observed around the annulus.

Figs. 9a to c show the difference between the local surface force for the axisymmetric case and the non-axisymmetric case under examination ($\frac{\phi^D_{local}(axi)}{q_{inf}}$ - $\frac{\phi^D_{local}(non-axi)}{q_{inf}}$) around the nacelle azimuth. With this definition, a positive value denotes a reduction of drag for the non-axisymmetric case and hence increase in net propulsive force. Note that in Figs. 9a to c it is the relative magnitude of

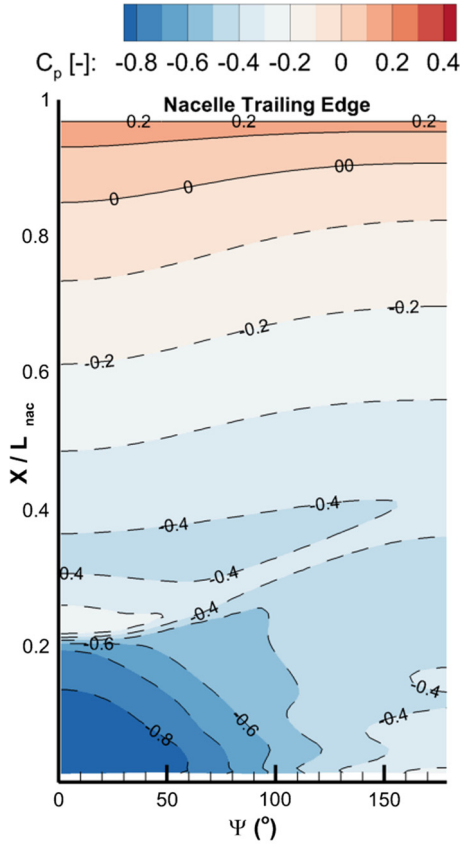


Fig. 8. Variation of Static Pressure Coefficient over the axisymmetric nacelle at $\alpha = 3°$ and $M_0 = 0.85$.

the local surface force between each plot that is important, rather than the absolute magnitude. The results from a radius ratio of 0.975 are not presented as the major aerodynamic features are the same for both radius ratios of 0.95 and 0.975.

Firstly, consider the difference in the local nacelle surface force between case B with a radius ratio of 0.95 and the axisymmetric baseline case at an incidence of 3° (Fig. 9a). Note that the local surface plot of Case B with a non-circular afterbody design is not presented in Fig. 9 as there are no significant differences when compared to the circular case. Along the forebody of the nacelle (from x/L_{nac} = 0.0 to x/L_{nac} = 0.37) the local surface force is very similar between the two cases and hence $\frac{\phi^{local}_{cowl}(axi)}{q_{inf}} - \frac{\phi^{local}_{cowl}(non-axi)}{q_{inf}}$ is broadly equal to zero (Fig. 9a). At the axial location of maximum radius (x/L_{nac} = 0.53) the non-axisymmetric case shows a peak increase in drag between $\psi = 0°$ and 60° and $\psi = 110$ and 180. However, along the afterbody of the nacelle (from x/L_{nac} = 0.7 to the trailing edge at x/L_{nac} =1.0) there is region of decreased drag relative to the axisymmetric case. When these local changes are integrated over the entire nacelle the net effect is a reduction in the modified nacelle drag for the non-axisymmetric case relative to the axisymmetric case.

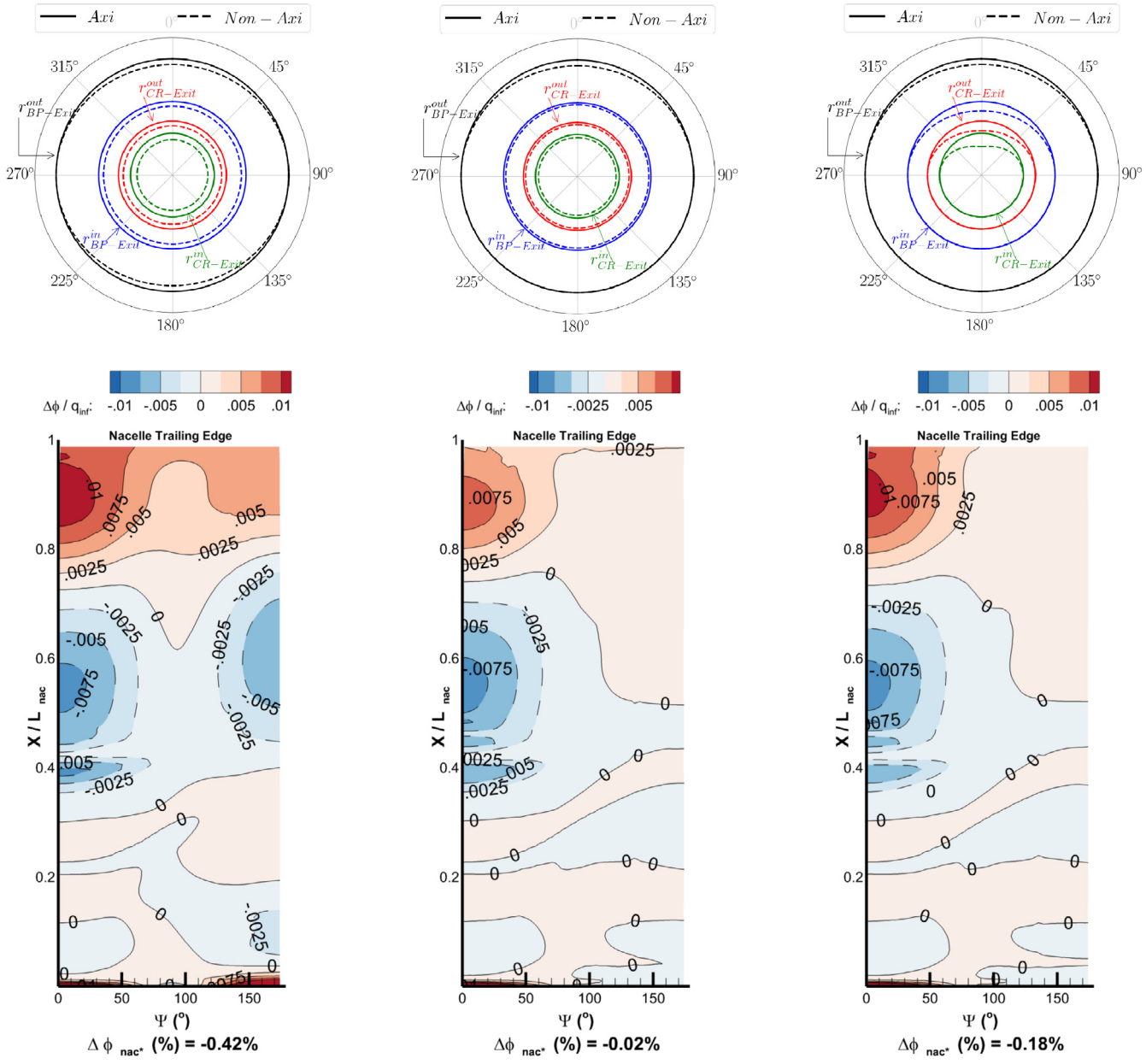
Between $\psi = 0°$ and 60° the local surface force distribution of case A with a radius ratio of 0.95 is very similar to that of case B (Fig. 9b compared to Fig. 9a). For case A there is no region of increased drag at $x/L_{nac} = 0.53$, $\psi = 180°$ as the bottom line geometry is the same as the axisymmetric case. That also means that for case A the region of reduced nacelle drag (from $x/L_{nac} = 0.7$ to the trailing edge at x/L_{nac} and between $\psi = 110°$ and 180°) is no longer present. Therefore, case A exhibits a reduction in NPF^D_c as the drag penalty at $x = 0.53$ between $\psi = 0°$ and 60° is therefore not avoided.

The variations in local surface force presented in Fig. 9 are dominated by changes to static pressure, as the viscous contribution to modified nacelle drag was found to be constant across the designs investigated. Therefore, reductions in modified nacelle drag arise due to an increase in static pressure along the afterbody of the nacelle. Such an increase in static pressure at the trailing edge of the nacelle is achieved through a reduction in the curvature of the post-exit streamline. The best example of this is mechanism is shown by the variation of modified nacelle drag between a circular and non-circular afterbody for case A (Figs. 9b and c).

For case A the design approach employed for the nozzle afterbody was shown to impact NPF^D_c by +0.24% with a radius ratio of 0.95. For a circular afterbody the penalty in NPF^D_c was 0.31% and for the non-circular afterbody the penalty was 0.07% (Fig. 7). The origin of this increase in NPF^D_c can be observed when $\frac{\phi^D_{local}(axi)}{q_{inf}} - \frac{\phi^D_{local}(non-axi)}{q_{inf}}$ is examined for the circular and non-circular cases (Figs. 9b and 9c). Whilst the overall shape of the $\frac{\phi^D_{local}(axi)}{q_{inf}} - \frac{\phi^D_{local}(non-axi)}{q_{inf}}$ distributions is broadly the same for the two nozzle designs, the magnitude of the drag reduction on the nacelle afterbody is higher for the non-circular case. This is shown by the peak value of $\frac{\phi^D_{local}(axi)}{q_{inf}} - \frac{\phi^D_{local}(non-axi)}{q_{inf}}$ on the nacelle from $x/L_{nac} = 0.7$ to $x/L_{nac} = 1.0$. The circular case had a peak value of 0.0075, with the non-circular case displaying a peak value of 0.01. This demonstrates that with a constant nacelle design, alterations to the exhaust afterbody effect the static pressure along the nacelle afterbody through variation in post-exit streamline curvature.

In a similar manner to Fig. 9, the variation in local surface force around the nacelle azimuth for designs with a radius ratio of 1.025 are shown in Fig. 10. As previously, Case B with a non-circular afterbody is not presented as the local force distribution was very similar to the case with a circular afterbody. All of the designs presented in Fig. 10 were found to have an increase modified nacelle drag compared to the axisymmetric baseline case and this increase can be observed through the local surface force distributions. Compared to the designs which employed radius ratios of 0.95, the topology of the local surface distribution is very similar but the polarity of the surface force change has been reversed. For example, Case B with a radius ratio of 1.025 and a circular afterbody design displays an increase in drag around the entire azimuthal along the afterbody of the nacelle ($x/L_{nac} = 0.8$ to 1.0) whereas with a radius ratio of 0.95 a reduction in drag was found over the same region (Fig. 10a compared to 9a). This increased drag arises due to a reduction in static pressure over the afterbody as the viscous force terms remained constant between the axisymmetric and non-axisymmetric designs. Furthermore, a region of drag reduction is present around the midbody of the nacelle ($x/L_{nac} = 0.35$ to 0.75) around the entire azimuth, but this drag reduction is not sufficient to outweigh the penalising effect on the afterbody of the nacelle.

For the Case A designs (Figs. 10b and c), the largest magnitude of the modified drag penalty associated with the increased radius ratio is located between $\psi = 0°$ and $\psi = 60°$ from $x/L_{nac} = 0.8$ to 1.0. As was the case for the radius ratio 0.95 case, the use of a non-circular afterbody design increases the magnitude of this change to the local surface force. Along the forebody of the nacelle (from $x/L_{nac} = 0$ to 0.4) all three of the 1.025 radius ratio designs exhibit a negligible change in surface force. The analysis of the local surface force suggests that the aerodynamic mechanism responsible for the changes to the modified nacelle drag is common to designs which feature both increases and decreases in radius ratio. Although all the designs with a radius ratio of 1.025 incur a penalty in modified drag, it should be noted that the Case A with both exhaust afterbody design produce an increased NPF^D_c rela-



(a) Case B with circular exhaust afterbody and radius ratio of 0.95

(b) Case A with circular exhaust afterbody and radius ratio of 0.95

(c) Case A with non-circular exhaust afterbody and radius ratio of 0.95

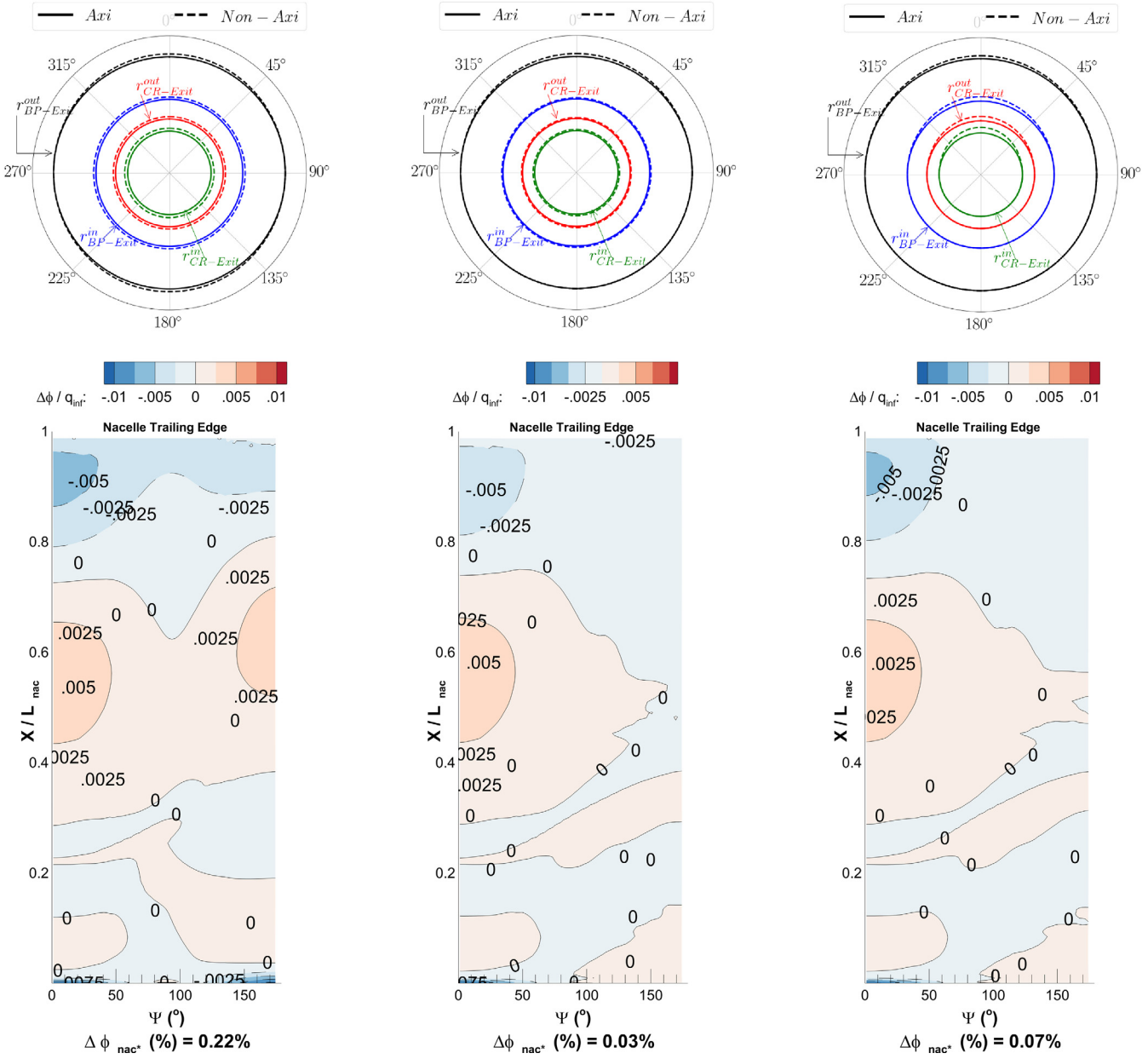
Fig. 9. Azimuthal variation of $\frac{\phi^D_{local}(axi)}{q_{inf}} - \frac{\phi^D_{local}(non-axi)}{q_{inf}}$ over the nacelle for three different bypass nozzle designs. Positive values (red) denote a reduction in drag for the non-axisymmetric case, and negative values (blue) denote an increase in drag relative to the axisymmetric nacelle. Engine-only configuration at $\alpha = 3°$ and $M_0 = 0.85$. (For interpretation of the colours in the figure(s), the reader is referred to the web version of this article.)

tive to the axisymmetric baseline due to the increased values of GPF^D_{c*}.

4. Conclusion

This paper has presented a novel design and analysis method for non-axisymmetric aero-engine exhaust systems. A fully parametric and analytical approach to the design of non-axisymmetric separate-jet exhaust systems has been established based on intuitive class shape transformation functions. The approach has been used to generate a range of exhaust geometries with azimuthal variation of multiple nozzle design parameters controlled by intuitive design variables. Furthermore, the design methodology outlined is sufficiently robust such that it can be deployed in an automated design space exploration environment.

At typical cruise conditions, the introduction of azimuthal variations to the bypass nozzle outer radius was shown to alter engine net propulsive force between 0.12% and −0.28% relative to an axisymmetric nozzle design. From this study, the best performing design featured a reduction of the topline and bottomline bypass nozzle outer radius by 5% relative to the sideline radius. The major benefit to net propulsive force due to non-circular bypass and core nozzles was manifested through a reduction in modified nacelle drag. This curtailment of modified nacelle drag arose due to a reduction in the post-exit streamline curvature and a concurrent increase in static pressure on the nacelle afterbody. As such, it can



(a) Case B with circular exhaust afterbody and radius ratio of 1.025

(b) Case A with circular exhaust afterbody and radius ratio of 1.025

(c) Case A with non-circular exhaust afterbody and radius ratio of 1.025

Fig. 10. Azimuthal variation of $\frac{\phi^D_{local}(axi)}{q_{inf}} - \frac{\phi^D_{local}(non-axi)}{q_{inf}}$ over the nacelle for three different bypass nozzle designs. Positive values (red) denote a reduction in drag for the non-axisymmetric case, and negative values (blue) denote an increase in drag relative to the axisymmetric nacelle. Engine-only configuration at $\alpha = 3°$ and $M_0 = 0.85$.

be concluded that the proposed design and analysis method represents an enabling technology for the design and installation of future high bypass ratio aero-engines.

Declaration of Competing Interest

There is no conflict of interest.

Acknowledgements

John J. Otter's doctoral studies were funded by Rolls-Royce plc. and the Engineering and Physical Sciences Research Council. The authors would like to thank Chris Sheaf for his insightful feedback and support of this publication. Furthermore, the authors would also like acknowledge Tomasz Stańkowski, Matthew Robinson and Santiago Ramírez Rubio for their work in establishing an automated meshing framework for aero-engine geometries. Due to commercial confidentiality agreements the supporting data is not available.

References

[1] J. Zhang, Z. Zhou, W. Wei, Y. Deng, Aerodynamic design of an ultra-low rotating speed geared fan, Aerosp. Sci. Technol. 63 (2017) 73–81.
[2] N.T. Birch, 2020 vision: the prospects for large civil aircraft propulsion, Aeronaut. J. August 2000 (2020) 347–352.
[3] A. Guha, Optimum fan pressure ratio for bypass engines with separate or mixed exhaust streams, J. Propuls. Power 17 (5) (2001) 1117–1122.

[4] I. Goulos, T. Stankowski, J. Otter, D. MacManus, N. Grech, C. Sheaf, Aerodynamic design of separate-jet exhausts for future civil aero-engines Part I: parametric geometry definition and computational fluid dynamics approach, J. Eng. Gas Turbines Power 138 (8) (2016), No. GTP-15-1538.
[5] K. Knowles, A.J. Saddington, A review of jet mixing enhancement for aircraft propulsion applications, Proc. Inst. Mech. Eng., G J. Aerosp. Eng. 220 (2) (2006) 103–127.
[6] R.C. Vermula, G. Valentich, R. Kumar, Flow Field Characteristics of Non-axisymmetric Jets at High Temperatures, AIAA Paper 2017-1888, 2017.
[7] K.B.M.Q. Zaman, Spreading Characteristics and Thrust of Jets From Asymmetric Nozzles, AIAA Paper 96-0200, 1996.
[8] F.J. Capone, The Nonaxisymmetric Nozzle – It Is for Real, AIAA Paper 79-1810, 1979.
[9] J.S. Lilley, Optimum geometries for scarfed perfect nozzles, J. Propuls. Power 7 (4) (1991) 586–592.
[10] P. Behrouzi, J.J. McGuirk, C. Avenell, Effect of scarfing on rectangular nozzle supersonic jet plume flow characteristics, AIAA J. 56 (1) (2018) 301–315.
[11] R.H. Thomas, K.W. Kinzie, Jet-Pylon Interaction of High Bypass Ratio Separate Flow Nozzle Configurations, AIAA Paper 2004-2827, 2004.
[12] D. Munday, M. Mihaescu, E. Gutmark, Experimental and numerical study of jets from elliptic nozzles with conic plug, AIAA J. 49 (3) (2011) 554–564.
[13] R.H. Thomas, Y. Guo, J.J. Berton, H. Fernandez, Aircraft Noise Reduction Technology Roadmap Toward Achieving the NASA 2035 Noise Goal, AIAA Paper 2017-3193, 2017.
[14] D. Papamoschou, New method for jet noise reduction in turbofan engines, AIAA J. 42 (11) (2004) 2245–2253.
[15] H. Hoheisel, Aerodynamic aspects of engine-aircraft integration of transport aircraft, Aerosp. Sci. Technol. 7 (1997) 475–487.
[16] B. Malouin, J.-Y. Trepanier, E. Laurendeau, Installation and interference drag decomposition via RANS far-field methods, Aerosp. Sci. Technol. 54 (2016) 132–142.
[17] R. Wilhelm, An inverse design method for engine nacelles and wings, Aerosp. Sci. Technol. 9 (1) (2005).
[18] D. Hue, C. Francois, J. Dandois, A. Gebhardt, Simulations of an aircraft with constant and pulsed blowing flow control at the engine/wing junction, Aerosp. Sci. Technol. 69 (2017) 659–673.
[19] Z. Zhu, N. Qin, Intuitive class/shape function parameterization for airfoils, AIAA J. 52 (1) (2014) 17–24.
[20] B.M. Kulfan, Universal parametric geometry representation method, J. Aircr. 45 (1) (2008) 142–158.
[21] B.M. Kulfan, Recent extensions and applications of the 'CST' universal parametric geometry representation method, Aeronaut. J. 114 (1153) (2010) 157–176.
[22] C. Liu, Y. Duan, J. Cai, J. Wang, Application of the 3D multi-block CST method to hypersonic aircraft optimization, Aerosp. Sci. Technol. 50 (2016).
[23] T. Zhang, Z. Wang, W. Huang, L. Yan, Parameterization and optimization of hypersonic-gliding vehicle configurations during conceptual design, Aerosp. Sci. Technol. 58 (2016).
[24] X. Wu, W. Zhang, X. Peng, Z. Wang, Benchmark aerodynamic shape optimization with the POD-based CST airfoil parametric method, Aerosp. Sci. Technol. 84 (2019) 632–640.
[25] R. Christie, A. Heidebrecht, D. MacManus, An automated approach to nacelle parameterization using intuitive class shape transformation curves, J. Eng. Gas Turbines Power 139 (6) (2016), No. GTP-16-1227.
[26] A. Heidebrecht, T. Stankowski, D. MacManus, Parametric geometry and CFD process for turbofan nacelles, in: Proceedings of ASME 2016 Turbo Expo: Turbomachinery Technical Conference and Exposition, 2016, pp. GT2016–57784.
[27] M. Robinson, D.G. MacManus, A. Heidebrecht, N. Grech, An Optimization Method for Nacelle Design, AIAA Paper 2017-0708, 2017.
[28] M. Robinson, D.G. MacManus, K. Richards, C. Sheaf, Short and Slim Nacelle Design for Ultra-High BPR Engines, AIAA Paper 2017-0707, 2017.
[29] A. Heidebrecht, D. MacManus, Surrogate model of complex non-linear data for preliminary nacelle design, Aerosp. Sci. Technol. 84 (2019).
[30] I. Goulos, J. Otter, T. Stankowski, D. MacManus, N. Grech, C. Sheaf, Aerodynamic design of separate-jet exhausts for future civil aero-engines Part II: design space exploration, surrogate modeling, and optimization, J. Eng. Gas Turbines Power 138 (8) (2016).
[31] I. Goulos, T. Stankowski, D. MacManus, P. Woodrow, C. Sheaf, Civil turbofan engine exhaust aerodynamic: impact of bypass nozzle after-body design, Aerosp. Sci. Technol. 73 (2018).
[32] Y. Lee, Yawei Ma, G. Jegdesh, Rolling-ball method and contour marching approach to identifying critical regions for complex surface machining, Comput. Ind. 41 (21) (2000) 163–180.
[33] MIDAP Study Group, Guide to In-Flight Thrust Measurement of Turbojets and Fan Engines, Advisory Group for Aerospace Research and Development, Paris, 1979, AGARDograph No. 237.
[34] T.P. Stankowski, D.G. MacManus, C.T. Sheaf, R. Christie, Aerodynamics of aero-engine installation, Proc. Inst. Mech. Eng., G J. Aerosp. Eng. 54 (2016).
[35] J. Otter, I. Goulos, D. MacManus, M. Slaby, Aerodynamic analysis of civil aero-engine exhaust systems using computational fluid dynamics, J. Propuls. Power 34 (5) (2018) 1152–1165.
[36] J.M. Weiss, J.P. Maruszewski, W.A. Smith, Implicit Solution of the Navier-Stokes Equations on Unstructured Meshes, AIAA Paper 97-2103, 1997.
[37] F.R. Menter, Two-equation eddy-viscosity turbulence models for engineering applications, AIAA J. 32 (8) (1994) 1598–1605.
[38] P. Walsh, P. Fletcher, Gas Turbine Performance, 2nd ed., Blackwell Publishing, Oxford, 2004.
[39] W. Sutherland, The viscosity of gases and molecular forces, Philos. Mag. 5 (36) (1893) 507–531.
[40] K.L. Mikkelsen, D.J. Myren, D.G. Dahl, M.D. Christiansen, Initial subscale performance measurements of the AIAA Dual Separate Flow Reference (DSFR) nozzle, in: 51st AIAA/SAE/ASEE Joint Propulsion Conference, 2015.
[41] Ansys, Canonsburg, PA, ANSYS FLUENT V15.0, 2013.
[42] P. Roache, Perspective: a method for uniform reporting of grid refinement studies, J. Fluids Eng. 116 (3) (1994) 405–413.
[43] P.J. Roache, Quantification of uncertainty in computational fluid dynamics, Annu. Rev. Fluid Mech. 29 (1997) 129–160.
[44] D.L. Daggett, S. Brown, R.T. Kawai, Ultra Efficient Engine Diameter Study, NASA, CR-2003-212309, 2003.



https://dspace.org/

Parametric design of non-axisymmetric separate-jet aero-engine exhaust systems

Otter, John J.; Christie, Robert; Goulos, Ioannis; MacManus, David G.; Grech, Nicholas

2019-07-16
Elsevier
https://doi.org/10.1016/j.ast.2019.05.038
Otter JJ, Christie R, et al., (2019) Parametric design of non-axisymmetric separate-jet aero-engine exhaust systems. Aerospace Science and Technology, Volume 93, October 2019, Article number 105186

Downloaded from a DSpace repository. https://dspace.org/